Electrochemical phase diagrams for Ti oxides from density functional calculations

Liang-Feng Huang and James M. Rondinelli*

Department of Materials Science and Engineering, Northwestern University, Evanston, Illinois 60208, USA

(Received 4 September 2015; revised manuscript received 17 November 2015; published 21 December 2015)

Developing an accurate simulation method for the electrochemical stability of solids, as well as understanding the physics related with its accuracy, is critically important for improving the performance of compounds and predicting the stability of new materials in aqueous environments. Herein we propose a workflow for the accurate calculation of first-principles electrochemical phase (Pourbaix) diagrams. With this scheme, we study the electrochemical stabilities of Ti and Ti oxides using density-functional theory. First, we find the accuracy of an exchange-correlation functional in predicting formation energies and electrochemical stabilities is closely related with the electronic exchange interaction therein. Second, the metaGGA and hybrid functionals with a more precise description of the electronic exchange interaction lead to a systematic improvement in the accuracy of the Pourbaix diagrams. Furthermore, we show that accurate Ti Pourbaix diagrams also require that thermal effects are included through vibrational contributions to the free energy. We then use these diagrams to explain various experimental electrochemical phenomena for the Ti–O system, and show that if experimental formation energies for Ti oxides, which contain contributions from defects owing to their generation at high (combustion) temperatures, are directly used to predict room temperature Pourbaix diagrams then significant inaccuracies result. In contrast, the formation energies from accurate first-principles calculations, e.g., using metaGGA and hybrid functionals, are found to be more reliable. Finally, to facilitate the future application of our accurate electrochemical phase equilibria diagrams, the variation of the Ti Pourbaix diagrams with aqueous ion concentration is also provided.

DOI: 10.1103/PhysRevB.92.245126 PACS number(s): 81.05.Bx, 81.05.Je, 82.45.Bb, 71.15.Mb

I. INTRODUCTION

The phase stability of transition metals and their native complex oxides under variable pH and potential bias is a foundational concept utilized for the design of functional materials in a variety of industries ranging from high-performing corrosion resistant alloys [1], superior electrode materials for energy storage systems [2,3], and biocompatibility of implants [1,4]. This fact is clear when considering Ti, which beyond being an important structural material owing to its excellent mechanical properties, has high corrosion resistance and high biocompatiblity, is lightweight, and readily alloys with others elements [4–9]. These features make it well suited for applications in aqueous and *in vivo* environments. Moreover, passivating Ti oxides enhance the corrosion resistance of metallic Ti [10], whereas titanate oxides such as TiO_2 have applications in pigmentation, sensors, solar cells, and photocatalysis (e.g., water splitting and pollutant treatment), derived from the oxides superior electronic and optical properties [11–14]. Nonetheless, the operational materials performance of Ti and its native oxides are in part limited by their electrochemical properties, specifically corrosion susceptibility, which can be understood from solid-aqueous phase equilibria diagrams.

The main materials chemistry tool to understand such thermodynamics includes the electrochemical Pourbaix diagram [15], which maps the response of pH and potential (V) on the phase stability of the metal, oxides, and/or hydroxides and ions in solution. Pourbaix diagrams may be directly generated by detailed and challenging electrochemical measurements [16,17]. However, it is often difficult to achieve a reliable Pourbaix diagram in one set (or several sets) of experimental measurements, because of challenges in controlled sample preparation and accurate characterization [18]. Alternatively, as is more common, Pourbaix diagrams are computed by using (a) the collected experimental formation energies [19–22] and/or (b) the calculated formation energies [23,24], which are described in more detail below. However, both experimental and theoretical formation energies are sometimes prone to inaccuracy owing to various causes, and the computed Pourbaix diagram may not be consistent with direct electrochemical measurements. Computational methods are also particularly sought for cases where new alloys and oxides are being developed, i.e., to enable predictive materials design, or for rapid phase space exploration as in cases where the potential phase space of candidate oxides and hydroxides is sufficiently large to make discerning various phases from experiment impractical.

The first computation approach mentioned above relies on experimental chemical potentials of aqueous ions at *room temperature* and the formation energies of oxides estimated from *high-temperature* combustion reactions. This information is then used as input into the relevant thermoelectrochemical equations to generate the solid-aqueous phase equilibria diagram. This approach, for example, was previously used to predict the Ti Pourbaix diagram; however, the resulting stability of various phases were found to be inconsistent with direct electrochemical measurements: TiO_2 was predicted to corrode under acid solutions with pH values of $\lesssim -1.0$ [15,22,25], while various electrochemical measurements show that the corrosion boundary of TiO_2 is at a pH value of 0.8–2.0 [10,26]. Furthermore, TiO appears at lower potentials than Ti_2O_3 in many Pourbaix diagrams simulated using this approach [15,22,23], whereas TiO is not observed in electrochemical measurements [10]. Such inconsistencies may be reconciled by understanding that the experimental formation

*jrondinelli@northwestern.edu

energies for oxides are estimated from heat of combustion reactions at high temperatures [27], where a high concentration of stoichiometric/nonstoichiometric defects are readily formed [11,28], and are known to significantly affect the oxide stability [28]. Accurately predicting the electrochemical stability of transition metals and oxides, such as Ti and Ti oxides at low (room) temperature, therefore, indicates that available experimental oxide formation energies obtained from high temperature measurements should probably be avoided.

The second computation approach averts this complication by utilizing first-principles calculations based on density functional theory (DFT) to compute the formation energies of the pristine oxides and combining the *ab initio* energies with experimental chemical potentials for ions in solution [23,24]. However, this introduces a different challenge: how accurate are the calculated formation energies of transition metals and their oxides? This accuracy depends on the ability of the exchange-correlation potential (V_{xc}) within the DFT formalism to produce the detailed balance of an ionocovalent metal-oxygen bond and to gives energies for reference state species that are close to experimental values. Within this context, the local density approximation (LDA) [29] and generalized gradient approximation (GGA) [30] are the two most frequently used semilocal density functionals, and their inaccuracies are well documented regarding the famous overbinding problem in the O_2 molecule [31,32] and the self-interaction error in transition-metal oxides [31,33].

To remove the inaccuracy of these functionals, various "fitting" corrections [33–38] to the energies of the reference species (O_2 and metal) or to the electronic potential for the oxides (Hubbard U correction [39]) are used to improve the agreement with experiment. Although these numerical corrections may be useful when fast calculations are required, e.g., in large-scale structural searches and high-throughput simulations, where relatively modest accuracies in total energies are acceptable for a meaningful result [40,41], they may result in an unphysically large U value. This is the case in titanate oxides [38,42], where values from $4 \leqslant U \leqslant 9$ eV are used for the $3d$ manifold, despite correlations typically being weak owing to the small valence orbital occupancy [12,42]. Furthermore, the experimental formation energies for which the DFT energies are corrected to achieve agreement may also introduce some additional inaccuracy owing to the contribution of the defect stabilizing effect in the experiments.

On the other hand, exchange-correlation functionals with a more sophisticated treatment of the *electronic exchange interaction*, through for example adding nonlocal electronic exchange (in metaGGA and hybrid functionals) to that of the homogeneous electron gas, can improve the thermodynamic stability, lattice constants, electronic properties, and phonon frequencies of transition metals and related compounds [14,42,43]. In transition metal oxides, the localized d orbital renders the electron density highly inhomogeneous and environment dependent, which results in an obvious nonlocal character of the electronic Hamiltonian, especially for the electronic exchange. This electronic exchange nonlocality is uniquely treated in both metaGGA and hybrid functionals, i.e., by using an additional electronic kinetic energy term and nonlocal Fock exchange, respectively. Such functionals could provide a more systematic path towards realizing meaningful predictions of electrochemical behavior. Nonetheless, the extent to which these functionals are better for simulating Pourbaix diagrams and the underlying mechanism governing their accuracy has yet to be reported.

Here we describe a streamlined first-principles workflow that combines DFT calculations without *ad hoc* corrections for the formation energies of solids with experimental chemical potentials of aqueous ions at standard state. We apply this scheme to study Ti and Ti oxides, focusing first on the functional dependence of these compounds to explain the connection between the electronic exchange interaction and the electronic structure. With this understanding, we justify the exchange-correlation functional dependence of the DFT calculated Ti Pourbaix diagrams and explain various experimental electrochemical phenomena with our accurate diagrams that include portions of exact-Fock exchange. Lastly, we examine the variation of the diagrams with aqueous ion concentration and inclusion of lattice vibrational factors in our simulations. Our work provides a framework for accurate *ab initio* simulations of transition-metal Pourbaix diagrams under different environmental conditions and provides updated and reliable Ti Pourbaix diagrams that are likely to be useful for both scientific research and industrial technologies.

II. MATERIALS AND THEORETICAL METHODS

A. Titanium materials system

The considered Ti oxides include Ti_6O, Ti_3O, Ti_2O, Ti_3O_2, TiO, Ti_2O_3, Ti_3O_5, Ti_4O_7, TiO_2 (rutile), and Ti_2O_7, the former four of which are oxides with interstitial O atoms, whereas some of the others with Ti_nO_{2n-1} stoichiometries correspond to the Magnéli phases. Except for Ti_3O_2 and Ti_2O_7, all structures are obtained from the *Inorganic Crystal Structure Database* [44]. Ti_3O_2 is obtained by placing one more O atom into Ti_3O from which we find from our DFT calculations (detailed next) that an AB-type stacking arrangement of interstitial O atoms is the most stable configuration. Ti_2O_7 is obtained from the *Materials Project* [45]. The structures obtained from these databases are used as the initial input for our simulations; the structural details of each are given in the Supplemental Material [46].

Note that more than 100 titanate oxide (Ti_mO_n) variants are reported experimentally [28] with variable oxygen content $x = n/(m+n)$ ranging from 0 to $\frac{2}{3}$. Here, we have selected the aforementioned compounds as representative of such phases, and those examined have oxygen concentrations spanning the same oxygen content range. The additional phases may be found in the *Inorganic Crystal Structure Database* [44], *Materials Project* [45], and *Open Quantum Materials Database* [47].

B. Computational methods

The structures and energies are calculated using DFT [48], which is implemented in the Vienna *Ab Initio* Package (VASP) [49–51]. The interaction among the core and valence electrons is treated using the projector augmented-wave (PAW) method [52,53]. The details of this separation of electrons may influence the formation energies involved in calculating the electrochemical phase diagrams. Indeed, Fig. 1(a) shows how

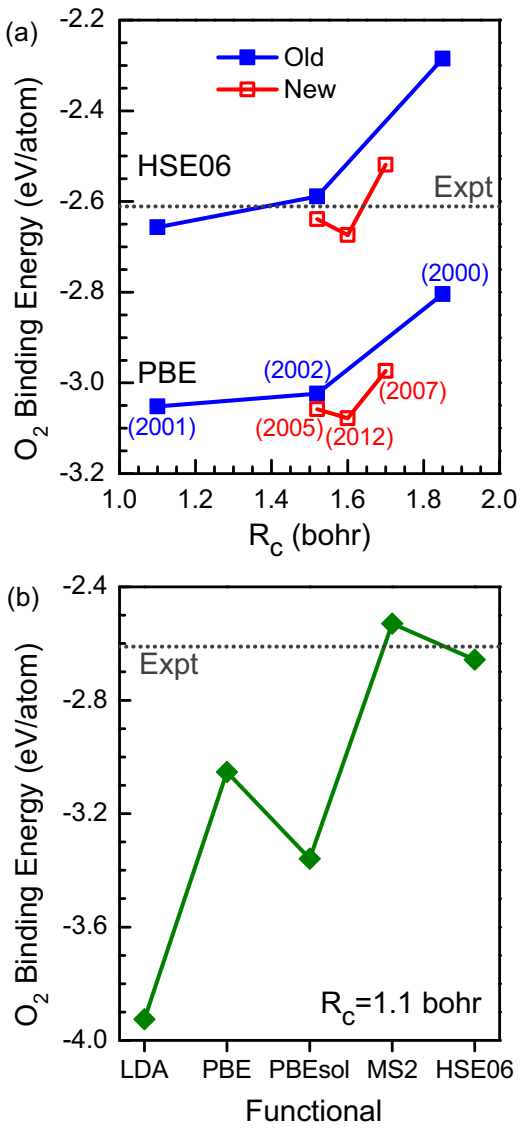

FIG. 1. (Color online) Dependence of the O_2 binding energy on the type of (a) pseudopotential and (b) density functional at $R_c = 1.1$ bohr, where R_c is the ion radius in the PAW pseudopotential. The zero-point energy correction (−0.049 eV) has been used in the experimental value (−2.611 eV). In panel (a), the generation years of the pseudopotentials provided by VASP are indicated in parentheses.

the O_2 binding energy [E_b (O_2)] depends on the PAW ion-core radius (R_c). By comparing our results with the hardest PAW pseudopotential ($R_c = 1.1$ bohr) used for different functionals, we find that PAWs with $R_c > 1.6$ bohr have a lower accuracy. For this reason, the hardest PAW pseudopotentials for the O (atomic configuration $2s^2 2p^4$; $R_c = 1.1$ bohr) and Ti ($3s^2 3p^6 3d^2 4s^2$; 2.3 bohr) atoms are used here, and a cutoff energy of 900 eV is used in the plane wave expansion to achieve an energetic convergence of <3 meV per atom. The reciprocal-space k-grid density is set to be $\gtrsim \frac{26}{a_0} \times \frac{26}{b_0} \times \frac{26}{c_0}$ for the calculation of Ti oxides, where a_0, b_0, and c_0 are lattice constants of the periodic cell scaled by the unit of angstrom. For pure metallic Ti, the grid is 1.5 times denser along each direction. The convergence threshold for the self-consistency electronic iteration is set to be 10^{-6} eV, which is required for accurate forces, stresses, and vibrational frequencies. The atomic positions, cell volume, and cell shape are globally optimized, where the convergence thresholds for energy, force, and stress are set to be 10^{-5} eV, 10^{-3} eV/Å, and 0.2 GPa, respectively.

To study the effect of electronic exchange, exchange-correlation functionals with different approximations along Jacob's ladder [54] are used and compared: (i) local density approximation (LDA), (ii) generalized gradient approximation (GGA), (iii) metaGGA, and (iv) hybrid functional. The LDA functional used here is parametrized by Perdew and Zunger [29], and the exchange-correlation interaction at a local site equals that of a homogeneous electron gas with the same electron density. Two functionals at the GGA level are used, i.e., PBE [30] and PBEsol [55]. PBE considers the electron-density inhomogeneity by including the density gradient, and PBEsol is derived by making the PBE exchange enhancement factor have the same asymptotic trend as the fully homogeneous gas given by the LDA. Note that the PBE functional is used to construct the PAWs for all DFT calculations that use the PBEsol, MS2, and HSE06 functionals, whereas the PAWs used in the LDA calculations are generated using the LDA functional.

Various functionals at the metaGGA level include TPSS [56], revTPSS [57], and MS2 [58], which mainly capture the nonlocal electronic exchange by additionally including electronic kinetic energy. Here we employ the MS2 potential owing to its higher numerical stability found in our benchmark calculations. Finally, the HSE06 hybrid functional [59] is used to study the effect of nonlocal electronic exchange, where 25% semilocal PBE electronic exchange is replaced by the exact Fock exchange, and a screening length of 10 Å is used for numerical convergence.

Note that no corrections to the formation energies of the oxides are made in this work, because such values can be obtained by using more accurate functionals which include sophisticated treatments of exact electronic exchange (described in detail in the Results section). For example, the O_2 binding is largely overestimated by the LDA, PBE, and PBEsol functionals [Fig. 1(b)], with the PBEsol $E_b(O_2)$ intermediate between the others, because the electronic exchange in PBEsol is intermediate between LDA and PBE [55]. However, the MS2 and HSE06 functionals with nonlocal electronic exchange interaction have an accuracy of <0.07 eV for $E_b(O_2)$ with respect to the experimental result. For this reason, no artificial correction is necessary for oxide E_f when functionals with more precise electronic exchange are included.

The phonon spectra are calculated using the small-displacement (or frozen phonon) method [60], which is implemented in the PHONOPY code [61]. The Ti and titanate oxide supercells used for the phonon calculations and a description of the relative performance of each functional in reproducing the experimental crystal structure are provided in the Supplemental Material [46]. To obtain accurate phonon band dispersions, there are two criteria that we have tried to fulfill: (1) the supercell lattice constants should be >9 Å and (2) both the Brillouin-zone center and boundary of the unit cell should be sampled by the supercell, i.e., the supercell lattice constants should be an even multiple of those of the unit cell. When these two criteria are not fulfilled, artificial imaginary vibrational modes sometimes (not always) appear.

TABLE I. Calculated formation energy (E_f) and vibrational free energy (F_{vib}) for Ti oxides. E_f is calculated using different density functionals, while F_{vib} is only calculated using LDA. F_{vib} is absent for TiO and Ti_2O_7, indicated by "–", owing to their dynamical instability at the LDA level. Note that there is a negligible functional dependence ($\lesssim$1.6 meV per Ti atom) up to room temperature on the vibrational energies (see Supplemental Material [46]); an error of <50 meV per Ti atom is unlikely to have a substantial influence on the calculated Pourbaix diagrams.

	E_f (eV/f.u.)					F_{vib} (eV/f.u.)	
	LDA	PBE	PBEsol	MS2	HSE06	0 K	298.15 K
Ti_6O	−6.64	−5.69	−6.06	−5.93	−6.33	0.34	0.11
Ti_3O	−6.49	−5.54	−5.90	−5.76	−5.99	0.23	0.12
Ti_2O	−6.30	−5.36	−5.70	−5.56	−5.65	0.18	0.11
Ti_3O_2	−12.23	−10.18	−10.95	−10.39	−10.69	0.34	0.23
TiO	−5.51	−4.52	−4.87	−4.50	−4.46	–	–
Ti_2O_3	−16.46	−14.28	−14.90	−14.62	−14.99	0.35	0.26
Ti_3O_5	−26.68	−23.35	−24.25	−24.01	−24.66	0.58	0.42
Ti_4O_7	−36.85	−32.32	−33.50	−33.34	−34.07	0.75	0.51
TiO_2	−10.14	−8.93	−9.23	−9.32	−9.43	0.21	0.14
Ti_2O_7	−18.66	−16.43	−16.72	−16.00	−16.51	–	–

Although the overbinding character of the LDA functional leads to some minor discrepancies in the lattice constant compared to experiment, the free energy always has a small functional dependence [62], which is also shown by the negligible functional dependence of the Ti free energy (see Supplemental Material [46]). Because the LDA functional has been shown to be highly accurate for describing the lattice dynamical and thermodynamic properties of both pure Ti and TiO_2 [63], we have selected to also use it here when including vibrational contributions to the free energy. We also note that we only consider free energies at room temperature, where both the small thermal expansion of a solid may be safely omitted and the temperature-dependent free energies are well described by harmonic phonons at fixed volumes (e.g., DFT equilibrium volumes). The accuracy of the theoretical harmonic LDA free energies are compared to experiment for Ti and TiO_2 in the Supplemental Material [46].

C. Thermodynamics

The formation energy (E_f) for a Ti oxide (e.g., Ti_mO_n) is calculated as

$$E_f = E_e(\mathrm{Ti}_m\mathrm{O}_n) - m\cdot E_e(\mathrm{Ti}) - \frac{n}{2}E_e(\mathrm{O}_2)\,, \qquad (1)$$

where E_e is the electronic total energy for the oxide, pure Ti metal in the HCP structure, and an isolated O_2 molecule, respectively, obtained from DFT. The calculated E_f's for various Ti oxides using different functionals are shown in Table I.

When simulating the electrochemical stability at room temperature (298.15 K), thermal contributions should be included for the chemical potential of the oxides as

$$\mu(\mathrm{Ti}_m\mathrm{O}_n) = E_f + \Delta F_{vib} - \frac{n}{2}\Delta F_T(\mathrm{O}_2)\,, \qquad (2)$$

TABLE II. Standard chemical potential (μ^0, in eV) of aqueous ions at 298.15 K obtained from four experimental databases. The Pourbaix and Bard's data (column 1) are used in this work. Burgess's and Lide's data are calculated from the redox potentials listed in the provided references.

Ion	Pourbaix and Bard [15,64]	Burgess [65]	Lide [66]
Ti^{++}	−3.26	−3.26	−3.26
Ti^{+++}	−3.63	−3.63	−4.16
$(TiO_2)^{++}$	−4.84	–	–
$(HTiO_3)^-$	−9.91	–	–
$(TiO)^{++}$	−5.98	–	–

where ΔF_{vib} is the contribution from the vibrational free energies of the Ti oxides (Table I) and pure metal [0.04 (0 K) and −0.01 (298.15 K) eV per Ti, respectively]. $\Delta F_T(O_2)$ is the free energy of O_2 gas at the standard state (298.15 K and 1.0 bar), which includes the contributions from the translation, rotation, and vibration of the O_2 molecule. $\Delta F_T(O_2)$ is 0.10 and −0.45 eV at 0 and 298.15 K, respectively. Often ΔF_{vib} is omitted in DFT simulations examining oxide stability owing to its expensive computational costs, however, we explicitly include it in this work.

Directly calculating the chemical potential of ions in solution is still challenging for DFT, however, the experimental standard chemical potentials (μ^0; 298.15 K and 1.0 mol/L) of various ions are well established. Ti^{++}, Ti^{+++}, $(TiO)^{++}$, and $(HTiO_3)^-$ are the most frequently observed Ti ions in solution; we have collected the chemical potentials for these ions from experimental databases in Table II. Note that the chemical potential of an aqueous ion (e.g., ion I) at a specified concentration ([I]) can be expressed as

$$\mu(\mathrm{I}) = \mu^0 + RT\ \log([\mathrm{I}]), \qquad (3)$$

where R is the gas constant [8.31446 J/(mol K)]. In addition, the experimental μ^0 for water is −2.458 eV [27].

D. Simulation method for Pourbaix diagram

The general workflow for our *ab initio* simulation of the electrochemical Pourbaix diagrams is shown in Fig. 2. It involves the use of thermodynamic principles, data from experimentation, and computed quantities from an electronic structure method. The involved steps are described in detail below using the Ti materials system, but the approach is readily transferred to other material families.

(1) The workflow starts at enumerating involved reaction species, e.g., metal, oxides, water, and aqueous ions, which is indicated by the first box in the "Thermodynamics" row of Fig. 2.

(2) Knowing the involved species, we construct the reaction paths that connect all of the species, and then derive the expressions of the reaction chemical potentials for these paths [see the "Formulate reaction chemical potentials ($\Delta\mu$)" box and Table III in the Appendix].

(3) On the other hand, the required solution data, i.e., ion chemical potentials, are aggregated upon knowing the involved species (see the "List data" box). Here the experimental

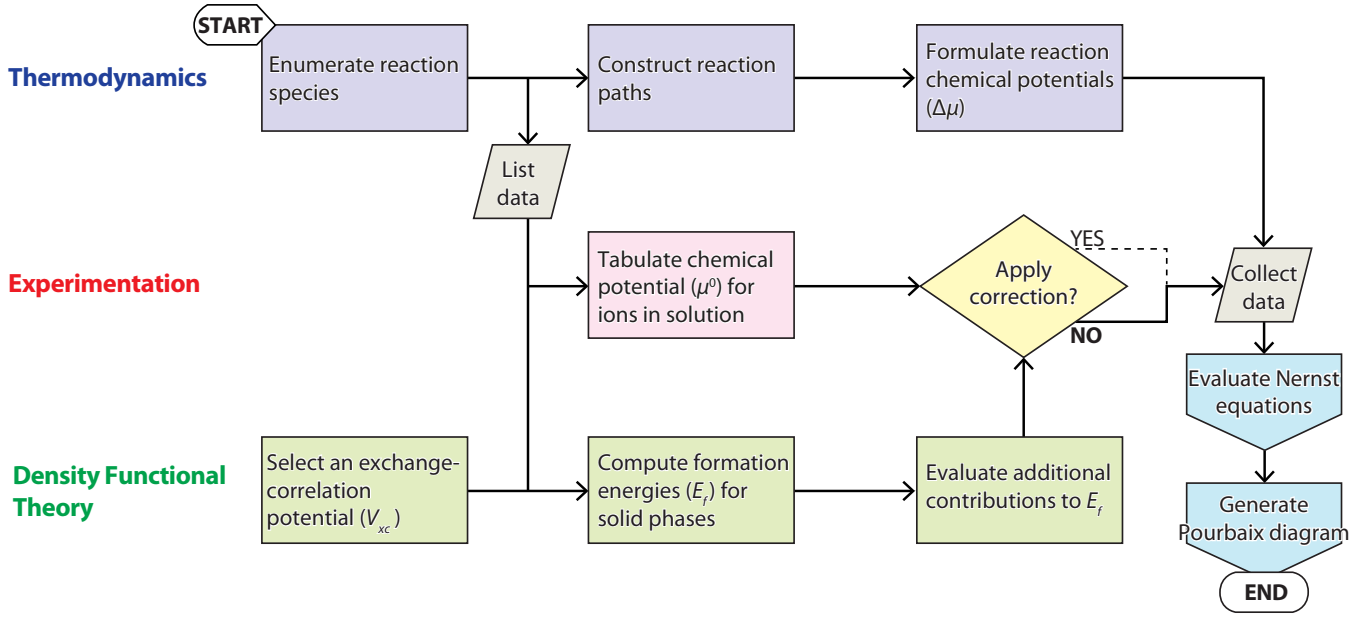

FIG. 2. (Color online) Workflow diagram for accurate (correction free) simulation of electrochemical Pourbaix diagrams from density functional theory. The process involves inputs from thermodynamic formula, experimental data, and accurate density functional theory. The path taken in this work follows the bolded arrows and further details for what occurs at each step are given in the main text. Of note, we point out that a variety of corrections can be made to improve the agreement between density functional theory values and experiment; however, we avoid these *ad hoc* (and often tedious) corrections by using more accurate functionals that include additional forms of electronic exchange. In the outcome step involving the Nernst equations, the chemical potential is computed with collected theoretical and experimental data for each species with respect to pH and electrode potential; the molar concentration of the aqueous ions in solution is also specified. In the final step, the lowest energy species per pH value and electrode potential is obtained on a dense grid to generate the resulting Pourbaix diagrams that appear throughout the text.

standard chemical potentials (μ^0) of aqueous ions in solution are used and tabulated in a subsequent step (Table II).

(4) Next, density functional theory is used to compute the formation energies of the Ti oxides (see "Compute E_f for solid phases" boxes), before which one selects an exchange-correlation functional (V_{xc}) for use in the DFT calculation. Importantly, the accuracy of the *ab initio* Pourbaix diagrams is mainly determined by the performance of V_{xc}.

(5) Having the calculated oxide formation energies, it may be necessary to consider other additional contributions, e.g., vibrations, defects, and impurities ("Evaluate additional contributions to E_f" box). Ti oxides can be readily contaminated by other elements (e.g., Fe and C) [14,28,67,68], and there are always abundant spontaneous nonstoichiometric and stoichiometric defects in Ti oxides, especially in TiO_x with $x = 0.5$–2.0 [11,14,28,42,69]. The impurities and defects may considerably influence the structure and stability [14,28,42] of Ti oxides. To avoid the complexity in doped and defective Ti oxides, these two contributions are not considered here. In contrast, vibrational contributions to the formation energy are explicitly included.

(6) After obtaining the chemical potentials for the aqueous ions [Step (3)] and oxide formation energies [Steps (4) and (5)], the calculated formation energies (and/or sometimes the experimental μ^0) may be corrected [23] to obtain an accurate dissolution energy for oxides (see the "Apply Correction" decision box). This kind of correction originates from the inaccuracy of the DFT calculation owing to the selected V_{xc} in Step (4). Here, we avoid using this artificial correction by using state-of-art density functionals that include additional forms of electronic exchange (see bold path labeled by "No").

(7) All thermoelectrochemical data are then collected and the $\Delta\mu$ for each reaction path is obtained by evaluating the corresponding Nernst expression at specified pH values and electrode potential V.

(8) To generate a Pourbaix diagram, a dense numerical grid (4000×4000, here) spanning the concerned two-dimensional pH–V phase space (pH $\in [-2,16]$, $V \in [-3,3]$ V here) is used, and the relative chemical potentials of all the species with respect to a reference species (e.g., pure Ti) are calculated at all grid points (1.6×10^7 points, here). This procedure allows us to identify the equilibrium state on each grid point and to accurately trace the evolution of the phase boundaries. Finally, a Pourbaix diagram is generated after scanning the complete numerical grid.

III. RESULTS AND DISCUSSION

A. Functional dependence of titanate formation energies

Owing to the importance of the exchange-correlation functional in accurately reproducing experimental formation energies of solids, we first consider in detail the electronic origin of the functionals' performance on Ti oxides. The calculated formation energies (E_f) per formula unit for the Ti oxides obtained with the LDA, PBE, PBEsol, MS2, and HSE06 functionals are listed in Table I. To enable a direct comparison, these formation energies per atom are plotted in Fig. 3(a), and a comparison between the values of E_f obtained

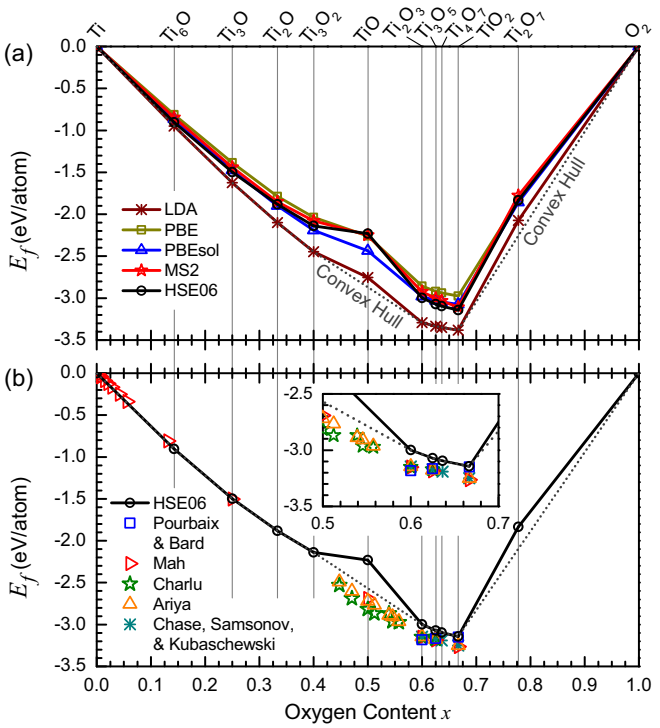

FIG. 3. (Color online) (a) Calculated formation energies (E_f) of Ti oxides with respect to various exchange-correlation potentials. (b) The comparison between HSE06 and experimental results [15,27,64]. The inset in panel (b) shows in detail the range $x \in (0.5,0.7)$.

with the HSE06 functional and available experimental values is given in panel (b).

First, we consider the general variation in formation energies obtained with local exchange-correlation functionals. The LDA functional [29] uses the exchange-correlation potential of the homogeneous electron gas, and has the famous overbinding problem for formation/binding energies of solids [30–32]. Thus the formation energies for all of the Ti oxides obtained from the LDA are the lowest among all the calculated results [Table I and Fig. 3(a)]. The PBE functional [30,70], which includes additional contributions of the electron density gradient, softens the bond strength between ions with respect to that predicted by the LDA [30]. Accordingly, the stability of the Ti oxides from PBE is 12%–18% lower than that from LDA. The PBEsol functional [55] enhances the stability of Ti oxides by 2%–8% with respect to PBE (see Table I), because the overbinding character of LDA is partially included in PBEsol.

Next, we consider the nonsemilocal functionals. Although PBEsol, MS2, and HSE06 functionals utilize different approaches to improve the accuracy of electronic exchange, all approximations decrease the formation energies for the Ti oxides with the exception that the values for TiO are larger from MS2 and HSE06 (Table I). For example, the difference between the PBE E_f(TiO) value and the corresponding convex hull is 0.2 eV/atom, which is significantly increased to be $\gtrsim$0.3 eV/atom by the MS2 and HSE06 functionals, but decreased to be $\sim$0.1 eV by the PBEsol functional (LDA functional) [Fig. 3(a)]. Since the electronic exchange in the PBEsol functional [55] is designed to be close to that of the LDA, the relative stability between different oxides obtained from the PBEsol functional is expected to differ from that predicted with the MS2 and HSE06 functionals.

Now we examine the variation in the formation energy of select oxides. The formation energies of Ti_2O_7 and TiO are clearly above the convex hull (Fig. 3), indicating their thermodynamic instability. In addition, they also have imaginary phonon modes (see Supplemental Material [46]), indicating their dynamical instability. The instability of Ti_2O_7 ($x = 0.78$) at the DFT level is understandable owing to the highest experimentally observed O content phase corresponding to $x = 0.67$ [28]. On the other hand, TiO has been widely measured in high-temperature oxidation experiments, and the experimental E_f(TiO) is quite close to the convex hull [Fig. 3(b)]. We note that, in our calculations for TiO, we have used a pristine cubic rocksalt structure; however, TiO is highly prone to stoichiometric/nonstoichiometric defects (even up to 25 at.% [28]), which transforms the ideal cubic TiO into the experimentally measured monoclinic phase [28,69,71]. It is these defects that stabilize the monoclinic TiO [28,42], and explain the existence of a "stable" TiO. To avoid the complex defect structures in TiO, we treat only the pristine case, and because it is not observed in electrochemical measurement at room temperature [10], where the stabilizing defects are difficult to form, we omit it as a candidate phase in the electrochemical phase diagrams below.

Defects are also widely observed and have a sensitive temperature dependence in the Magnéli phases (Ti_2O_3, Ti_3O_5, and Ti_4O_7) and TiO_2. The former phases also can be viewed as Ti oxides with a different density of extended defects [28], which results in a continuous variation of x from 0.40 to 0.67 as observed in experimental samples [28,69,73]. Indeed, the calculated HSE06 formation energies for Ti_2O_3, Ti_3O_5, Ti_4O_7, and TiO_2 are higher than the experimental ones by $\lesssim$0.1 eV per atom [Fig. 3(b)]. This discrepancy is likely a result of the high temperatures measurements. Lastly, for the interstitial oxides with $x \leqslant 0.25$, the discrepancy between the convex hull and experimental formation energies at the HSE 06 level is only 0.00–0.02 eV per atom, indicating the high accuracy of the hybrid functional.

B. Electronic structure dependencies

To understand the electronic scale origin of the functional dependence in more detail, we examine the radial electron density defined as

$$\rho_r = \frac{1}{4\pi r^2} \int_{|\mathbf{r}|=r} \rho(\mathbf{r}) d\mathbf{r}, \tag{4}$$

where $\mathbf{r}$ is the position vector (r is its length), and $\rho(\mathbf{r})$ is the electron density at the $\mathbf{r}$ point. ρ_r is the average electron density on a spherical surface with radius of r. Throughout we take the position of an O atom as the origin. According to the O concentration and lattice type, the interstital oxides (e.g., Ti_6O, Ti_3O, Ti_2O, and Ti_3O_2 here) and octahedral oxides (e.g., Ti_2O_3, Ti_3O_5, Ti_4O_7, TiO_2 here) are separated by rocksalt TiO. To derive a generic electronic structure mechanism, Ti_6O, TiO, and TiO_2 are then selected to analyze the functional dependence of ρ_r, with each serving

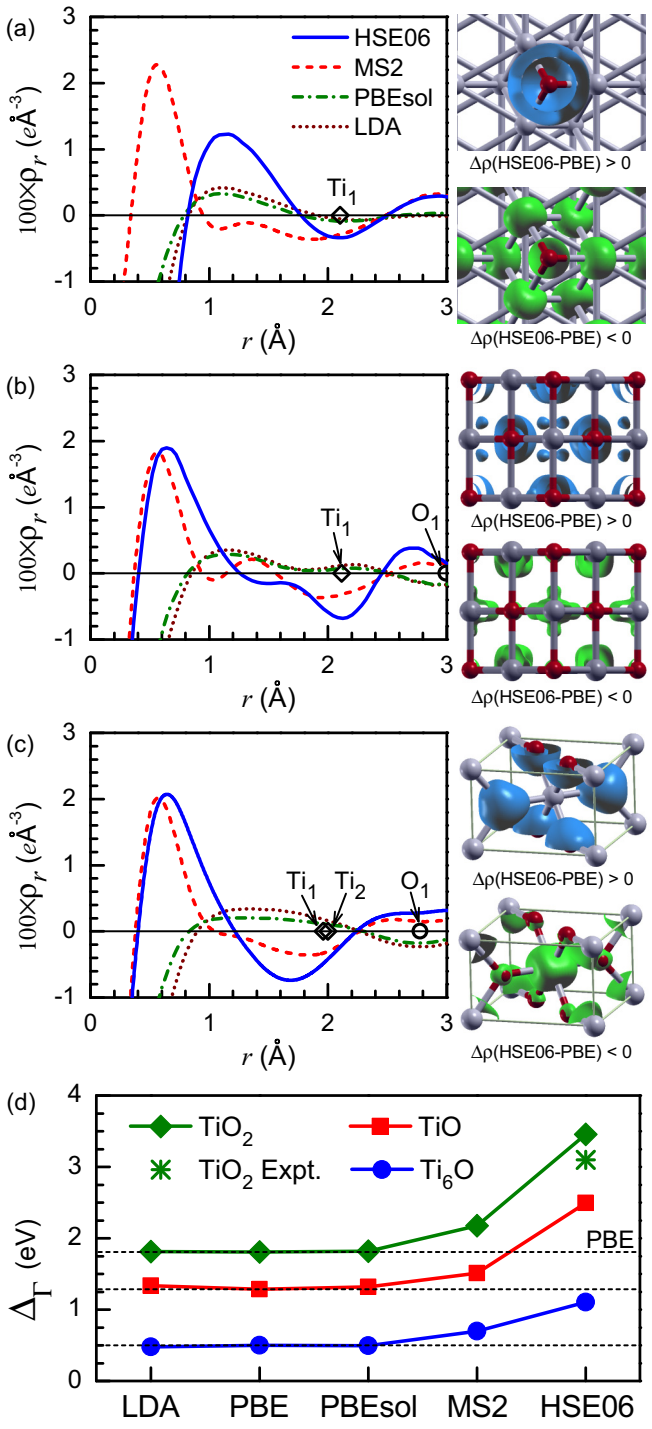

FIG. 4. (Color online) Functional-dependent radial electron density (ρ_r) around an O atom (reference: PBE ρ_r) and the electron density difference $\Delta\rho$ (HSE06-PBE) (isovalue: $\pm 0.01\ e\,\text{Å}^{-3}$) in (a) Ti_6O, (b) TiO, and (c) TiO_2, where the locations of the Ti and O neighbors for an O atom located at the origin (0 Å) are indicated by hollow diamonds and circles, respectively. (d) The functional-dependent Γ-point band gap (Δ_Γ) in Ti_6O, TiO, and TiO_2, where the PBE gaps are indicated by dashed horizontal lines, and the experimental Δ_Γ for rutile TiO_2 [11,14,69,72] is indicated by the star.

as a prototypical member of the interstitial, octahedral, and boundary oxides, respectively.

The calculated radial electron densities for Ti_6O, TiO, and TiO_2 are shown in Figs. 4(a)–4(c), accompanied by the three-dimensional electron density difference maps between PBE and HSE06, $\Delta\rho$(HSE06-PBE). We find from ρ_r and $\Delta\rho$(HSE06-PBE) that, compared with the PBE functional, the MS2 and HSE06 functionals draw more electrons from both O and Ti atoms into an interstitial shell region surrounding the O atom, which is expected to increase the bond covalency and bond strength. For example in rutile TiO_2 [Fig. 4(c)], the peak of ρ_r(HSE06-PBE) at 0.6 Å and the corresponding positive shell in $\Delta\rho$(HSE06-PBE) both indicate the increase in electrons participating in the Ti-O bond by nonlocal electronic exchange. Interestingly, the PBEsol functional does not considerably increase the electron density along the bond (dash-dotted line); its ρ_r is nearly the same as that of the LDA functional (dotted line) as seen in Fig. 4, because the LDA electronic exchange is partially used in the PBEsol functional [55].

The increased bond covalency also can be reflected by the increase in band gap. The band gap at the Γ point [Δ_Γ, Fig. 4(d)] is nearly the same from the LDA, PBE, and PBEsol functionals, due to the similar bond covalency, however, it is observably higher at both the MS2 and HSE06 levels owing to the increased bond covalency. The phase stability always increases with bond covalency in covalent systems. Therefore, we can conclude that the enhanced oxide stability obtained from the MS2 and HSE06 functional with respect to the PBE functional is mainly driven by the increased bond covalency, whereas the enhanced oxide stability from the PBEsol functional originates from the partial LDA overbinding character in PBEsol and not from a physically more precise electronic interaction. The former observation leads to a more accurate band gap of TiO_2 with the HSE06 functional compared to experiment [Fig. 4(d)], and such functionals with exact exchange are likely to give more accurate physical properties [14,43,75–78]. The latter then indicates that the relative accuracy of PBEsol in the formation energies for Ti oxides are coincidental, and a systematic accuracy for PBEsol is not guaranteed. For example, PBEsol $E_b(O_2)$ is inaccurate [Fig. 1(b)]. Thus we conclude that the PBEsol functional should be used with care for transition-metal oxide formation energies in the future.

C. Electrochemical phase diagrams

We now show how the changes in electronic structure alter the phase stability of competing oxides phases, and, in turn, modify the stability ranges in the electrochemical diagrams. The simulated Pourbaix diagrams using LDA, PBE, PBEsol, MS2, and HSE06 functional, as well as HSE06 functional plus vibrational contribution (HSE06 + vib), are shown in Fig. 5. Here, the ion concentration is set to be a moderate value of 10^{-6} mol/L. We also plot in each diagram the thermodynamic stability ranges for water, i.e., the phase space between its reduction ($2H^+ + 2e^- \rightarrow H_2$) and oxidation ($2H_2O \rightarrow O_2 + 4H^+ + 4e^-$) boundaries. The valence band maximum (VBM) of rutile TiO_2 is also given. It is higher in potential than the water oxidation boundary, and its conduction band minimum (CBM) is lower than the water reduction boundary. Thus light-induced electron-hole pairs in TiO_2 can generate high enough voltages to decompose water (into H_2 and O_2 gases) or other organic molecules. This is the

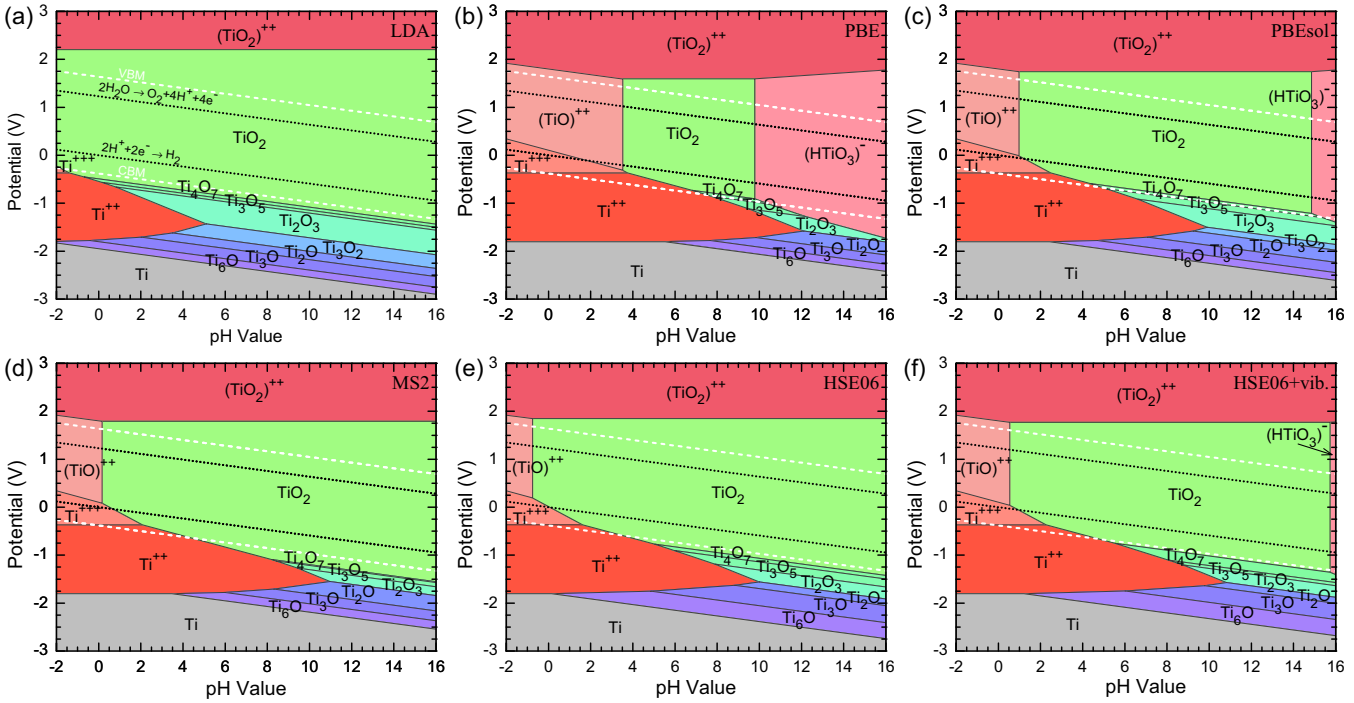

FIG. 5. (Color online) Pourbaix diagrams calculated using (a) LDA, (b) PBE, (c) PBEsol, (d) MS2, and (e) HSE06 functionals, as well as (f) HSE06 functional plus vibrational (vib) contributions. The CBM and VBM levels of rutile TiO_2, and the electrode potentials for the oxidation of H_2O to $O_2(2H_2O \rightarrow O_2 + 4H^+ + 4e^-)$ and for the reduction of H^+ to $H_2(2H^+ + 2e^- \rightarrow H_2)$ are obtained from Ref. [74].

reason why TiO_2 is a promising photocatalyst for hydrogen production and pollutant elimination [11,12,14,23,26,74].

For all cases in Fig. 5, the phase space can be divided into three kinds of domains [15]: (*i*) *immunity* ("I") domain with pure Ti metal, (*ii*) *passivation* ("P") domain with Ti oxides, and (*iii*) *corrosion* ("C") domain with aqueous ions. The phase spaces for the considered species always vary with the type of used V_{xc}, although some general trends in these Pourbaix diagrams may be drawn as follows: (1) as a base metal (not a noble metal), pure Ti is not stable at zero electrode potential, and the *immunity* domain may only be accessed by a negative electrode potential (e.g., < -1.84 V), (2) metal Ti will be directly corroded into aqueous ions in strong enough acid solutions, while in alkaline solutions, an oxide layer is expected to passivate the metal surface and protect the metal from corrosion, and (3) at high enough electrode potential (e.g., >1.77 V), the aqueous ion (e.g., TiO_2^{++}) will be the preferred state. Note that the slopes of the phase boundaries are determined by the number of electrons and H^+ ions involved in the reaction (see Table III in the Appendix), and the boundary heights are determined by the formation energies.

Before discussing the results of our simulations, we first summarize relevant electrochemical experiments as a guide to which phases are stable under variable pH and potential; this understanding will then be used to draw distinctions among the phase diagrams generated with different exchange-correlation functionals. TiO_2 is dissolved in acid solutions with pH value of 0.3–0.8 [26], whereas it is stable in solution with pH value of 2.0–11.0 [26]. Furthermore, Ti is spontaneously dissolved in solution when the pH value is <2.3–3.0, at which an oxide layer is assumed to exist and cover the Ti surface [10], indicating that the passivating oxide layer starts to be dissolved in strong acidic solutions and fails to protect the Ti metal. Thus the corrosion boundaries of TiO_2 should be at pH values of $\sim$1.5 under acid conditions and >11.0 under alkaline condition, respectively. Lastly, TiO_2 is stable in dilute acid solutions; for example, an acidic solution with pH $\sim$ 4.5 is used in industry to remove Fe compounds in rutile-structured minerals and synthesize high-purity rutile TiO_2 products [67,68].

In the Ti Pourbaix diagram calculated at the LDA level [Fig. 5(a)], the $(TiO)^{++}$ and $(HTiO_3)^-$ aqueous ions are absent under acid and alkaline conditions (pH $\in [-2,16]$), respectively, in constrast to experiment. The simulated $TiO_2 - Ti^{+++}$ (at zero potential) and TiO_2–$(TiO)^{++}$ boundaries reside at pH values of less than -2.0, while the experimental dissolution boundary of TiO_2 resides at a pH of $\sim$1.5 [10,26]. This incorrect simulated phase stability is due to the overestimated stability of Ti oxides by the LDA functional (Fig. 3).

In contrast, the PBE functional overcorrects that error, and the corrosion boundaries for TiO_2 into the Ti^{+++}, $(TiO)^{++}$, and $(HTiO_3)^-$ aqueous ions are at pH values of 2.1, 3.5, and 9.7, respectively, in the PBE Pourbaix diagram [Fig. 5(b)]. However, from the experimental observations [10,26], TiO_2 should be stable within the pH range of [2.0,11.0]. The phase spaces of other Ti oxides are also significantly reduced in the PBE Pourbaix diagram [Fig. 5(b)] compared with the LDA Pourbaix diagram [Fig. 5(a)]. The reduction in the phase stability of Ti oxides is driven by the underestimated stability of Ti oxides by the PBE functional (Fig. 3). Owing to this oxide stability reduction by the PBE functional, the PBE *immunity* and *corrosion* domains are considerably larger than the LDA ones. In an early simulated Pourbaix diagram of Ti that fully uses the experimental formation energies for

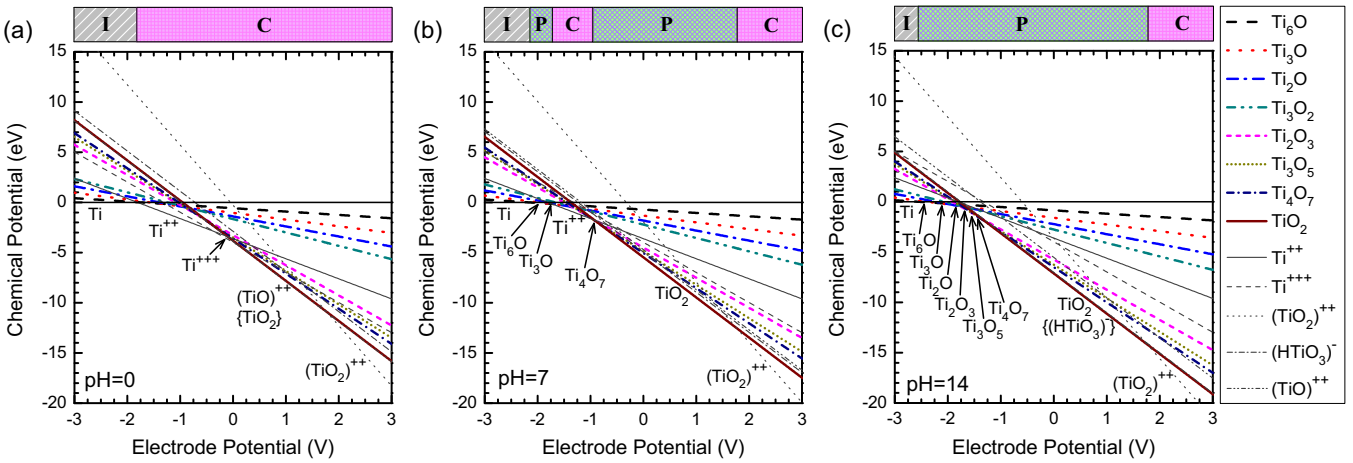

FIG. 6. (Color online) Variation of chemical potentials (μ) with electrode potential at different pH values (0, 7, and 14) calculated from the HSE06 + vib method, where μ(Ti) is the reference. The species with the lowest μ are labeled, and in panels (a) and (c), TiO_2 and $(HTiO_3)^-$ ion (in braces) are very close to the lowest TiO^{++} and $(TiO_2)^{++}$ ions, respectively. The immunity (**I**), passivation (**P**), and corrosion (**C**) domains are indicated on the panel top.

oxides and aqueous ions [15,22], the $(TiO)^{++}$ ion is absent in the Pourbaix diagram, and the $TiO_2 - Ti^{+++}$ boundary at zero potential resides at a pH values of approximately less than -1.0, which is also obviously incorrect compared with the experimental dissolution boundary $\sim$1.5 [10,26]. This incorrect prediction in electrochemical stability should be ascribed to the direct usage of the oxide formation energies derived from high-temperature combustion, which include some contributions from abundant defects.

In the PBEsol, Ms2, and HSE06 Pourbaix diagrams [Figs. 5(c)–5(e)], the dissolution pH values for TiO_2 into: (i) Ti^{+++} aqueous ion at zero electrode potential are 1.1, 0.5, and 0.0, respectively, (ii) $(TiO)^{++}$ aqueous ions (at any electrode potential) are 1.0, 0.2, and -0.8, respectively, and (iii) $(HTiO_3)^-$ aqueous ions (at any electrode potential) are $\gtrsim$15.0. The electrochemical stability of TiO_2 in acidic solutions is well studied in experiment; thus we focus on it here to evaluate the accuracy of these functionals. From the acid dissolution boundary of TiO_2, these results are in better agreement with experiment and are an improvement on the diagrams computed using the LDA and PBE exchange-correlation functionals. Although the $(HTiO_3)^-$ aqueous ion only appears in strong acidic solution for the PBEsol Pourbaix diagram, whereas it is absent in the MS2 and HSE06 Pourbaix diagrams, its observation is supported by its precipitation mechanism (described below).

Comparing the HSE06 and HSE06 + vib Pourbaix diagrams [Figs. 5(e) and 5(f)], we find that including the oxide vibrational free energy contributions shifts the oxide corrosion boundaries [into Ti^{++}, Ti^{+++}, and $(TiO)^{++}$ aqueous ions] up to larger pH values by $\sim$1.0, and also makes $(HTiO_3)^-$ aqueous ion appear at strong alkaline condition in the Pourbaix diagram. The phase stability ranges of other Ti oxides are partially replaced by those of Ti^{++} and pure Ti. The phonons have a negative contribution to the oxide stability, because the vibrational correction to the chemical potential [$\Delta F_{\rm vib}$ in Eq. (2)] is positive (Table I). The vibrational correction shifts the pH values of the $TiO_2 - Ti^{+++}$ and $TiO_2 - (TiO)^{++}$ boundaries upwards by 0.7 and 1.3, respectively. Therefore, the vibration-corrected $TiO_2 - Ti^{+++}$ boundary resides at pH values of 1.8, 1.2, and 0.7 in the PBEsol, MS2, and HSE06 Pourbaix diagrams, respectively, and the vibration-corrected $TiO_2 - (TiO)^{++}$ boundary resides at pH values of 2.3, 1.5, and 0.5, respectively. All of these boundary pH values are very close to the experimental dissolution boundary for TiO_2 mentioned above (pH $\sim 0.8 - 2.0$). Note that the accuracy achieved by the PBEsol functional in our Pourbaix diagram is accidental as described before. Because the metaGGA MS2 functional requires much less CPU time than a hybrid (HSE06) functional, but yields accurate $E_b(O_2)$ (Fig. 1), oxide E_f's (Fig. 3), and therefore Pourbaix diagram (Fig. 5), we propose that it should be used for future calculations of nonmagnetic materials when computational efficiency without *ad hoc* corrections is required.

The variations of chemical potentials (μ) with electrode potential are shown in Fig. 6, where the pH values of 0, 7, and 14 are considered, respectively. These results are obtained from the HSE06 + vib method, but note that similar conclusions for the phase stability trends are obtained from the other functionals. These variations of μ not only present the underlying energetic mechanism for the evolution in the phase stability described in the Pourbaix diagrams, but also suggest the precipitation probability of some species. Upon decreasing the electrode potential, there is a well-defined stability order for the oxides at any pH value (from most to least stable):

$$TiO_2 \rightarrow Ti_4O_7 \rightarrow Ti_3O_5 \rightarrow Ti_2O_3 \rightarrow \\ \rightarrow Ti_2O(\gtrsim Ti_3O_2) \rightarrow Ti_3O \rightarrow Ti_6O\,,$$

which is also observed in the Pourbaix diagrams in Fig. 5 by moving along the axis of electrode potential. This stability order for TiO_2 and the Magnéli phases is consistent with electrochemical experiments, and among these phases, Ti_2O_3 also has been measured to be the oxide stable at the lowest electrode potential [10].

Comparing the upper panels of Fig. 6, it can be explicitly seen that the *passivation* domain expands with increasing pH value, because of the downshift of oxide chemical potentials

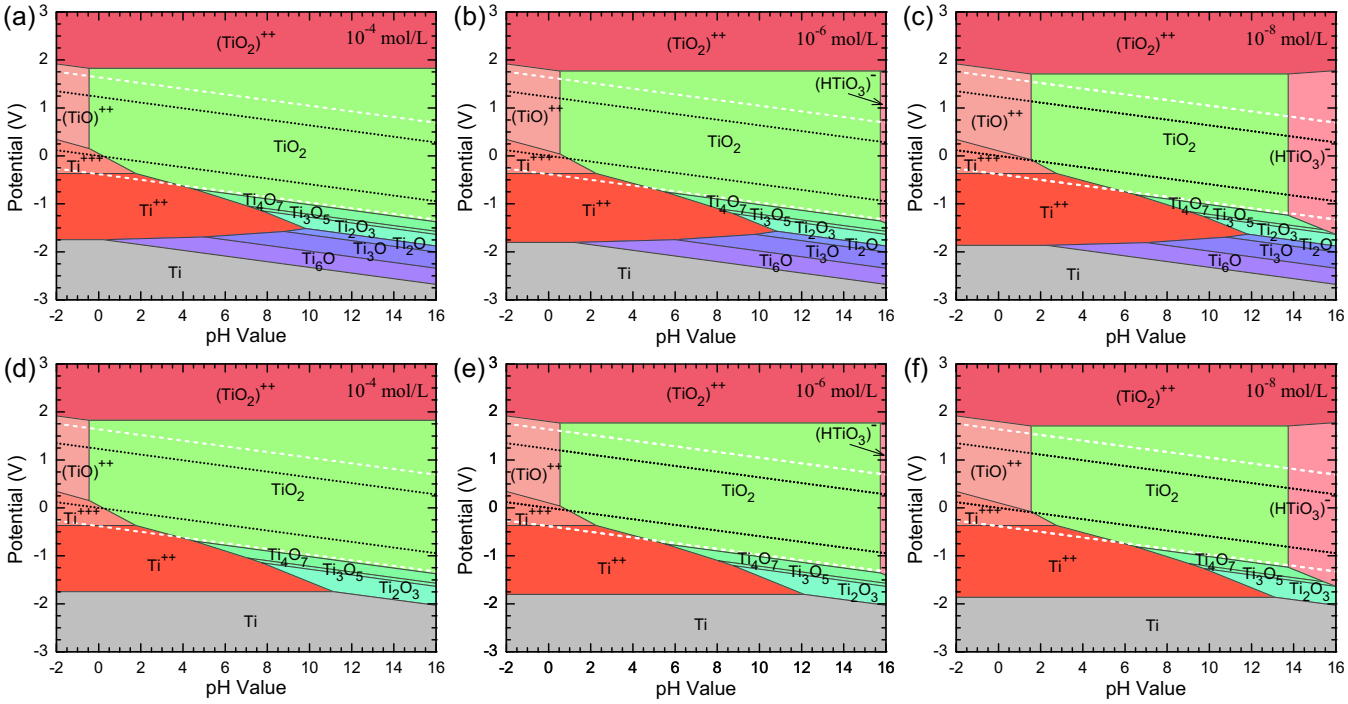

FIG. 7. (Color online) Pourbaix diagrams with aqueous ion concentrations of (a), (d) 10^{-4}, (b), (e) 10^{-6}, and (c), (f) 10^{-8} mol/L, obtained with the HSE06 + vib method. The interstitial oxides are excluded in panels (d) through (f).

with respect to those of the aqueous ions and pure Ti. This oxide stabilization is due to the decreased number of H^+ ions available to react with Ti oxides (see the Appendix). Interestingly, the interstitial oxides have not been observed in electrochemical experiments [10]. This can be explained by recognizing that the intercalation of O atoms into the HCP Ti lattice requires overcoming a high diffusion barrier (>2.0 eV) [79], and thus there is likely insufficient time for the ordered interstitial oxides to form on the surface of metal Ti at room temperature. (Pourbaix diagrams without the interstitial oxide phases are given in Fig. 7.) TiO also has not been observed in electrochemical experiments in solutions at 298.15 K [10]. As discussed above, TiO has been widely observed in high-temperature phase diagrams (oxygen content: 0.40–0.55) [28,69,71], owing to the stabilization effect from the abundant defects formed at high temperatures. At room temperature, there is no such defect formation mechanism, which explains the absence of TiO in electrochemical experiments.

In acidic solution with pH = 0 [Fig. 6(a)], Ti^{++}, Ti^{+++}, $(TiO)^{++}$, and TiO_2 have very similar chemical potential values at the zero electrode potential. The latter two are also close for all electrode potential values. These energetics can be used to justify why amorphous TiO_2 controllably precipitates from a suspension solution of $TiCl_4$ and $Ti(OC_2H_5)$ at pH values around ∼0.3 [26]. Under acidic conditions, TiO_2 is a little more stable than the Magnéli phases (Ti_2O_3, Ti_3O_5, and Ti_4O_7) at zero electrode potential, which may be the reason why TiO_2 is observed as an intermediate phase during the dissolution of Ti_3O_5 in strong disulphuric solution [80].

With increasing pH value from 0 [Fig. 6(a)] to 7 [Fig. 6(b)], metal Ti is more protected by the passivating oxide, while only at a high electrode potential (>1.77 V), metal Ti or Ti oxides will be corroded into $(TiO_2)^{++}$ aqueous ions. This can be seen from the evolution in the chemical potentials in Fig. 6(b), and in the simplified stability regimes depicted in the upper panel. In the alkaline solution with pH = 14 [Fig. 6(c)], metal Ti is highly passivated upon increasing the electrode potential before being fully corroded into $(TiO_2)^{++}$ ions.

In the HSE06 + vib Pourbaix diagram [Fig. 5(f)], although the $(HTiO_3)^-$ aqueous ion only becomes the lowest chemical potential specie at very strong alkaline conditions (pH $\gtrsim$ 15.5), it nonetheless can easily precipitate at a relatively weaker alkaline condition (e.g., precipitation probability $\gtrsim 10^{-3}$ at pH $\gtrsim$ 12.7), because of its comparable chemical potential with respect to TiO_2 in alkaline solution [Fig. 6(c)]. This precipitation mechanism should be responsible for the observation of aqueous $(HTiO_3)^-$ ions in experiment. Note that TiO_2 is found to be quite stable in alkaline solutions for pH values up to 11.0 [10,26], because those solutions are still not alkaline enough for an obvious precipitation of aqueous ions.

We now examine the variation of the Pourbaix diagrams on the aqueous-ion concentration [from 10^{-4} to 10^{-8} mol/L, Figs. 7(a)–7(c)]. A 10^{-4} mol/L solution has a relatively large aqueous ion concentration, whereas 10^{-8} mol/L corresponds to very high purity water, e.g., nuclear reactor water [20]. We find that upon decreasing the ion concentration by a factor of 10^2, the pH values for the $TiO_2 - Ti^{++}$, $TiO_2 - Ti^{+++}$, $TiO_2 - (TiO)^{++}$, and $TiO_2 - (HTiO_3)^-$ boundaries change by about 0.5, 0.5, 1.0, and −2.0, respectively, because of the lower chemical potentials of these species at lower concentration [see Eq. (3)]. However, the electrode potentials for the dissolution (and passivation) boundaries of Ti oxides (metal Ti) have no obvious variation (<0.1 V from 10^{-4} to 10^{-8} mol/L).

Pourbaix diagrams omitting the interstitial oxides not observed experimentally are shown in Figs. 7(d)–7(f). The excluded passivation domains with interstitial oxides are

mainly replaced by the *immunity* domain with metal Ti, and partially replaced by the *corrosion* domain with Ti^{++} aqueous ion. The boundary pH values have similar variations with ion concentration as those described above when the interstitial oxides are explicitly included. The Pourbaix diagrams with interstitial oxides [Figs. 7(a)–7(c)] are useful in the experimental/theoretical studies when there is any factor (e.g., catalyst) that facilitates the oxygen diffusion in pure Ti and then promotes the formation of interstitial oxides on Ti surface, while the Pourbaix diagrams without interstitial oxides [Figs. 7(d)–7(f)] are ideally suited for conventional electrochemical studies.

IV. CONCLUSION

We formulated an *ab initio* workflow for accurate simulation of the electrochemical phase equilibria under variable pH and potential, where vibrational effects are also taken into account. The protocol was applied to the Ti–O system, whereby the formation energies of Ti oxides and Ti Pourbaix diagrams were systematically calculated using semilocal (LDA, PBE, and PBEsol), metaGGA (MS2), and hybrid (HSE06) density functionals. This comparative simulation approach uncovered the correlation between the simulated electrochemical stability accuracy (determined by consistency with experimental observations) and the electronic-exchange precision in the exchange-correlation functional used within the DFT framework. The stability variations were then explained by the density-functional dependent electronic structure in the oxides.

Various experimental phenomena that have been inconsistent with previous calculated Ti Pourbaix diagrams were also explained by and become consistent with our most accurate Pourbaix diagram obtained using the HSE06 functional plus vibrational contributions. Furthermore, we found that when the experimental formation energies of Ti oxides estimated from combustion heats, which include contributions from defects that inevitably form at high temperatures, are directly used to predict low-temperature Pourbaix diagrams, then significant inaccuracies are likely to result. The Ti oxides obtained from high-temperature combustion may accommodate $\lesssim$25 at.% defects, which will additionally stabilize the oxides by $\lesssim$0.35 eV/atom. In low-temperature electrochemical environments, however, there is insufficient thermal activation for defect generation. Thus, rather than using the experimental formation energies, more accurate MS2 and HSE06 formation energies may be used as representative of "true" formation energies for pristine Ti oxides in the future. These accurate *ab initio* predicted Pourbaix diagrams obtained using advanced exchange-correlation functionals without any *ad hoc* corrections are expected to be useful for both scientific and industrial exploitation for the design of high-performing corossion resistant alloys, energy storage materials, and biocompatible implants.

ACKNOWLEDGMENTS

L.-F.H. and J.M.R. wish to thank Professor J.R. Scully (University of Virginia), Dr. Qimin Yan (Lawrence Berkeley National Laboratory), and Professor L.D. Marks (Northwestern University) for insightful discussions. L.-F.H. and J.M.R. were supported by the Office of Naval Research MURI "Understanding Atomic Scale Structure in Four Dimensions to Design and Control Corrosion Resistant Alloys" under Grant No. N00014-14-1-0675. Calculations were performed using the QUEST HPC Facility at Northwestern University and the HPCMP facilities at the Navy DoD Supercomputing Resource Center.

APPENDIX: REACTION PATHS AND REACTION ENERGIES

In aqueous environments, the relative electrochemical stability between various species (e.g., metal, oxides, and aqueous ions) are calculated from the reaction chemical potentials ($\Delta\mu$) for the reactions paths that connect all of them. The considered reaction paths used for the Ti–O system and the associated reaction $\Delta\mu$'s are listed in Table III.

TABLE III. Reaction paths and the corresponding reaction energies ($\Delta\mu$, in kJ/mol), where μ(Ti) and $\mu(H^+)$ are the references (i.e., zero) for the chemical potentials at standard condition, and the standard hydrogen potential is the reference for the electrode potential U_p (in V). F is the Faraday constant ($=eN_A = 9.65 \times 10^4$ C mol^{-1}), and 1.0 kJ/mol $= F$ eV.

Reaction path	$\Delta\mu$
$Ti \longrightarrow Ti^{++} + 2e^-$	$\Delta\mu(Ti - Ti^{++}) = \mu(Ti) - \mu(Ti^{++}) + 2FU = -\mu(Ti^{++}) + 2FU_p$
$Ti^{+++} + e^- \longrightarrow Ti^{++}$	$\Delta\mu(Ti^{+++} - Ti^{++}) = \mu(Ti^{+++}) - \mu(Ti^{++}) - FU_p$
$(HTiO_3)^- + 5H^+ + 2e^- \longrightarrow Ti^{++} + 3H_2O$	$\Delta\mu(HTiO_3{}^- - Ti^{++}) = \mu(HTiO_3{}^-) - \mu(Ti^{++}) - 3\mu(H_2O) - 5RT\ln(10)\cdot pH - 2FU_p$
$(TiO_2)^{++} + 4H^+ + 4e^- \longrightarrow Ti^{++} + 2H_2O$	$\Delta\mu(TiO_2{}^{++} - Ti^{++}) = \mu(TiO_2{}^{++}) - \mu(Ti^{++}) - 4RT\ln(10)\cdot pH - 4FU_p$
$(TiO)^{++} + 2H^+ + 2e^- \longrightarrow Ti^{++} + H_2O$	$\Delta\mu(TiO^{++} - Ti^{++}) = \mu(TiO^{++}) - \mu(Ti^{++}) - \mu(H_2O) - 2RT\ln(10)\cdot pH - 2FU_p$
$\frac{1}{6}Ti_6O + \frac{1}{3}H^+ \longrightarrow Ti^{++} + \frac{1}{6}H_2O + \frac{5}{3}e^-$	$\Delta\mu(Ti_6O - Ti^{++}) = \frac{1}{6}\mu(Ti_6O) - \mu(Ti^{++}) - \frac{1}{6}\mu(H_2O) - \frac{1}{3}RT\ln(10)\cdot pH + \frac{5}{3}FU_p$
$\frac{1}{3}Ti_3O + \frac{2}{3}H^+ \longrightarrow Ti^{++} + \frac{1}{3}H_2O + \frac{4}{3}e^-$	$\Delta\mu(Ti_3O - Ti^{++}) = \frac{1}{3}\mu(Ti_3O) - \mu(Ti^{++}) - \frac{1}{3}\mu(H_2O) - \frac{2}{3}RT\ln(10)\cdot pH + \frac{4}{3}FU_p$
$\frac{1}{2}Ti_2O + H^+ \longrightarrow Ti^{++} + \frac{1}{2}H_2O + e^-$	$\Delta\mu(Ti_2O - Ti^{++}) = \frac{1}{2}\mu(Ti_2O) - \mu(Ti^{++}) - \frac{1}{2}\mu(H_2O) - RT\ln(10)\cdot pH + FU_p$
$\frac{1}{3}Ti_3O_2 + \frac{4}{3}H^+ \longrightarrow Ti^{++} + \frac{2}{3}H_2O + \frac{2}{3}e^-$	$\Delta\mu(Ti_3O_2 - Ti^{++}) = \frac{1}{3}\mu(Ti_3O_2) - \mu(Ti^{++}) - \frac{2}{3}\mu(H_2O) - \frac{4}{3}RT\ln(10)\cdot pH + \frac{2}{3}FU_p$
$\frac{1}{2}Ti_2O_3 + 3H^+ + e^- \longrightarrow Ti^{++} + \frac{3}{2}H_2O$	$\Delta\mu(Ti_2O_3 - Ti^{++}) = \frac{1}{2}\mu(Ti_2O_3) - \mu(Ti^{++}) - \frac{3}{2}\mu(H_2O) - 3RT\ln(10)\cdot pH - FU_p$
$\frac{1}{3}Ti_3O_5 + \frac{10}{3}H^+ + \frac{4}{3}e^- \longrightarrow Ti^{++} + \frac{5}{3}H_2O$	$\Delta\mu(Ti_3O_5 - Ti^{++}) = \frac{1}{3}\mu(Ti_3O_5) - \mu(Ti^{++}) - \frac{5}{3}\mu(H_2O) - \frac{10}{3}RT\ln(10)\cdot pH - \frac{4}{3}FU_p$
$\frac{1}{4}Ti_4O_7 + \frac{7}{2}H^+ + \frac{3}{2}e^- \longrightarrow Ti^{++} + \frac{7}{4}H_2O$	$\Delta\mu(Ti_4O_7 - Ti^{++}) = \frac{1}{4}\mu(Ti_4O_7) - \mu(Ti^{++}) - \frac{7}{4}\mu(H_2O) - \frac{7}{2}RT\ln(10)\cdot pH - \frac{3}{2}FU_p$
$TiO_2 + 4H^+ + 2e^- \longrightarrow Ti^{++} + 2H_2O$	$\Delta\mu(TiO_2 - Ti^{++}) = \mu(TiO_2) - \mu(Ti^{++}) - 2\mu(H_2O) - 4RT\ln(10)\cdot pH - 2FU_p$

[1] J. R. Davis, *Corrosion: Understanding the Basics* (ASM International, Materials Park, OH, 2000).

[2] P. Saha, M. K. Datta, O. I. Velikokhatnyi, A. Manivannan, D. Alman, and P. N. Kumta, Prog. Mater. Sci. **66**, 1 (2014).

[3] L. Kanevskii and V. Dubasova, Russ. J. Electrochem. **41**, 1 (2005).

[4] M. Geetha, A. K. Singh, R. Asokamani, and A. K. Gogia, Prog. Mater. Sci. **54**, 397 (2009).

[5] C. Leyens and M. Peters, *Titanium and Titanium Alloys. Fundamentals and Applications* (Wiley-VCH, Weinhein, 2003).

[6] G. Lütjering and J. C. Williams, *Titanium* (Springer, Berlin, 2007).

[7] D. Banerjee and J. C. Williams, Acta Mater. **61**, 844 (2013).

[8] M. Niinomi, Metall. Mater. Trans. A **33**, 477 (2002).

[9] X.-L. Yuan, M.-A. Xue, W. Chen, and T.-Q. An, Front. Phys. **9**, 219 (2014).

[10] E. J. Kelly, *Modern Aspects of Electrochemistry* (Springer, New York, 1982), pp. 319–424.

[11] F. A. Grant, Rev. Mod. Phys. **31**, 646 (1959).

[12] S. D. Mo and W. Y. Ching, Phys. Rev. B **51**, 13023 (1995).

[13] M. Lazzeri, A. Vittadini, and A. Selloni, Phys. Rev. B **63**, 155409 (2001).

[14] J. Muscat, V. Swamy, and N. M. Harrison, Phys. Rev. B **65**, 224112 (2002); A. Janotti, J. B. Varley, P. Rinke, N. Umezawa, G. Kresse, and C. G. Van de Walle, *ibid.* **81**, 085212 (2010); D. A. H. Hanaor and C. C. Sorrell, J. Mater. Sci. **46**, 855 (2011).

[15] M. Pourbaix, *ATLAS of Electrochemical Equilibria in Aqueous Solutions* (Pergamon Press, Oxford, 1966).

[16] I.-J. Yang, Mater. Chem. Phys. **49**, 50 (1997).

[17] A. T. Al-Hinai, M. H. Al-Hinai, and J. Dutta, Mater. Res. Bull. **49**, 645 (2014).

[18] R. Kelly, J. Scully, D. Shoesmith, and R. Buchheit, *Electrochemical Techniques in Corrosion Science and Engineering*, Corrosion Technology (CRC Press, Boca Raton, FL, 2002).

[19] B. Beverskog and I. Puigdomenech, Corros. Sci. **38**, 2121 (1996).

[20] B. Beverskog and I. Puigdomenech, Corros. Sci. **39**, 969 (1997).

[21] B. Beverskog and I. Puigdomenech, Corros. Sci. **39**, 107 (1997).

[22] M. J. Muñoz Portero, J. García-Antón, J. L. Guiñón, and R. Leiva-García, Corros. Sci. **53**, 1440 (2011).

[23] K. A. Persson, B. Waldwick, P. Lazic, and G. Ceder, Phys. Rev. B **85**, 235438 (2012).

[24] Z. Zeng, M. K. Y. Chan, Z. J. Zhao, J. Kubal, D. Fan, and J. Greeley, J. Phys. Chem. C **119**, 18177 (2015).

[25] T. Devic and C. Serre, Chem. Soc. Rev. **43**, 6097 (2014).

[26] H. Yin, Y. Wada, T. Kitamura, S. Kambe, S. Murasawa, H. Mori, T. Sakata, and S. Yanagida, J. Mater. Chem. **11**, 1694 (2001); N. Kröger, M. B. Dickerson, G. Ahmad, Y. Cai, M. S. Haluska, K. H. Sandhage, N. Poulsen, and V. C. Sheppard, Angew. Chem. Int. Ed. **45**, 7239 (2006); Y. Hu, M. Barbour, and G. Allen, in *4th European Conference of the International Federation for Medical and Biological Engineering*, IFMBE Proceedings, edited by J. Vander Sloten, P. Verdonck, M. Nyssen, and J. Haueisen (Springer, Berlin, 2009), Vol. 22, pp. 2265–2268; Z. Yigit and H. Inan, Water Air Soil Pollut.: Focus **9**, 237 (2009); N. Lee, D. A. Sverjensky, and R. M. Hazen, Environ. Sci. Technol. **48**, 9358 (2014).

[27] M. W. Chase, *NIST-JANAF Thermochemical Tables*, 4th ed. (American Institute of Physics, New York, 1998).

[28] J. L. Murray and H. A. Wriedt, Bull. Alloy Phase Diagrams **8**, 148 (1987); S. Bartkowski, M. Neumann, E. Z. Kurmaev, V. V. Fedorenko, S. N. Shamin, V. M. Cherkashenko, S. N. Nemnonov, A. Winiarski, and D. C. Rubie, Phys. Rev. B **56**, 10656 (1997); C. Leung, M. Weinert, P. B. Allen, and R. M. Wentzcovitch, *ibid.* **54**, 7857 (1996).

[29] D. M. Ceperley and B. J. Alder, Phys. Rev. Lett. **45**, 566 (1980); J. P. Perdew and A. Zunger, Phys. Rev. B **23**, 5048 (1981).

[30] J. P. Perdew, K. Burke, and M. Ernzerhof, Phys. Rev. Lett. **77**, 3865 (1996); **78**, 1396 (1997).

[31] R. O. Jones and O. Gunnarsson, Rev. Mod. Phys. **61**, 689 (1989).

[32] A. A. Adllan and A. Dal Corso, J. Phys.: Condens. Matter **23**, 425501 (2011).

[33] L. Wang, T. Maxisch, and G. Ceder, Phys. Rev. B **73**, 195107 (2006).

[34] S. Lany, Phys. Rev. B **78**, 245207 (2008).

[35] A. Jain, G. Hautier, S. P. Ong, C. J. Moore, C. C. Fischer, K. A. Persson, and G. Ceder, Phys. Rev. B **84**, 045115 (2011).

[36] S. Lutfalla, V. Shapovalov, and A. T. Bell, J. Chem. Theory Comput. **7**, 2218 (2011).

[37] V. Stevanović, S. Lany, X. Zhang, and A. Zunger, Phys. Rev. B **85**, 115104 (2012).

[38] M. Aykol and C. Wolverton, Phys. Rev. B **90**, 115105 (2014).

[39] V. I. Anisimov, J. Zaanen, and O. K. Andersen, Phys. Rev. B **44**, 943 (1991); A. I. Liechtenstein, V. I. Anisimov, and J. Zaanen, *ibid.* **52**, R5467 (1995); S. L. Dudarev, G. A. Botton, S. Y. Savrasov, C. J. Humphreys, and A. P. Sutton, *ibid.* **57**, 1505 (1998); V. I. Anisimov, F. Aryasetiawan, and A. I. Lichtenstein, J. Phys.: Condens. Matter **9**, 767 (1997); O. Bengone, M. Alouani, P. Blöchl, and J. Hugel, Phys. Rev. B **62**, 16392 (2000); A. Rohrbach, J. Hafner, and G. Kresse, J. Phys.: Condens. Matter **15**, 979 (2003).

[40] G. Hautier, C. C. Fischer, A. Jain, T. Mueller, and G. Ceder, Chem. Mater. **22**, 3762 (2010).

[41] A. Jain, G. Hautier, C. J. Moore, S. P. Ong, C. C. Fischer, T. Mueller, K. A. Persson, and G. Ceder, Comput. Mater. Sci. **50**, 2295 (2011).

[42] B. J. Morgan and G. W. Watson, Surf. Sci. **601**, 5034 (2007); J. Phys. Chem. C **114**, 2321 (2010); Z. Hu and H. Metiu, *ibid.* **115**, 5841 (2011); M. E. Arroyo-de Dompablo, A. Morales-Garca, and M. Taravillo, J. Chem. Phys. **135**, 054503 (2011); B. Jiang, G. Zhou, K. Huang, J. Hou, S. Jiao, and H. Zhu, Physica B **421**, 110 (2013).

[43] J. Paier, M. Marsman, and G. Kresse, Phys. Rev. B **78**, 121201 (2008); V. L. Chevrier, S. P. Ong, R. Armiento, M. K. Y. Chan, and G. Ceder, *ibid.* **82**, 075122 (2010); J. Yan and J. K. Nørskov, *ibid.* **88**, 245204 (2013); A. Dal Corso, J. Phys.: Condens. Matter **25**, 145401 (2013); M. Aras and C. Kilic, J. Chem. Phys. **141**, 044106 (2014); B. Medasani, M. Haranczyk, A. Canning, and M. Asta, Comput. Mater. Sci. **101**, 96 (2015).

[44] A. Belsky, M. Hellenbrandt, V. L. Karen, and P. Luksch, Acta Crystallogr., Sect. B **58**, 364 (2002).

[45] A. Jain, S. P. Ong, G. Hautier, W. Chen, W. D. Richards, S. Dacek, S. Cholia, D. Gunter, D. Skinner, G. Ceder, and K. A. Persson, APL Mater. **1**, 011002 (2013); the online database can be found on https://materialsproject.org.

[46] See Supplemental Material at http://link.aps.org/supplemental/10.1103/PhysRevB.92.245126 for crystal structure information, lattice dynamical information, and comparison of the calculated and experimental free energies of Ti and TiO_2.

[47] J. Saal, S. Kirklin, M. Aykol, B. Meredig, and C. Wolverton, JOM **65**, 1501 (2013); the online database can be found on http://oqmd.org.
[48] R. M. Martin, *Electronic Structure: Basic Theory and Practical Methods* (Cambridge University Press, Cambridge, UK, 2004).
[49] G. Kresse and J. Furthmüller, Comput. Mater. Sci. **6**, 15 (1996).
[50] G. Kresse and J. Furthmüller, Phys. Rev. B **54**, 11169 (1996).
[51] J. Hafner, J. Comput. Chem. **29**, 2044 (2008).
[52] P. E. Blöchl, Phys. Rev. B **50**, 17953 (1994).
[53] G. Kresse and D. Joubert, Phys. Rev. B **59**, 1758 (1999).
[54] J. P. Perdew and K. Schmidt, *Density Functional Theory and its Application to Materials*, edited by V. Van Doren, C. Van Alsenoy, and P. Geerlings, AIP Conf. Proc. No. 577 (AIP, New York, 2001), p. 1.
[55] J. P. Perdew, A. Ruzsinszky, G. I. Csonka, O. A. Vydrov, G. E. Scuseria, L. A. Constantin, X. Zhou, and K. Burke, Phys. Rev. Lett. **100**, 136406 (2008); **102**, 039902(E) (2009).
[56] J. Tao, J. P. Perdew, V. N. Staroverov, and G. E. Scuseria, Phys. Rev. Lett. **91**, 146401 (2003).
[57] J. P. Perdew, A. Ruzsinszky, G. I. Csonka, L. A. Constantin, and J. Sun, Phys. Rev. Lett. **103**, 026403 (2009).
[58] J. Sun, R. Haunschild, B. Xiao, I. W. Bulik, G. E. Scuseria, and J. P. Perdew, J. Chem. Phys. **138**, 044113 (2013); J. Sun, B. Xiao, Y. Fang, R. Haunschild, P. Hao, A. Ruzsinszky, G. I. Csonka, G. E. Scuseria, and J. P. Perdew, Phys. Rev. Lett. **111**, 106401 (2013).
[59] J. Heyd, G. E. Scuseria, and M. Ernzerhof, J. Chem. Phys. **118**, 8207 (2003); J. Heyd and G. E. Scuseria, *ibid.* **120**, 7274 (2004); **121**, 1187 (2004); J. Heyd, G. E. Scuseria, and M. Ernzerhof, *ibid.* **124**, 219906 (2006); O. A. Vydrov, J. Heyd, A. V. Krukau, and G. E. Scuseria, *ibid.* **125**, 074106 (2006).
[60] G. Kresse, J. Furthmüller, and J. Hafner, Europhys. Lett. **32**, 729 (1995); K. Parlinski, Z.-Q. Li, and Y. Kawazoe, Phys. Rev. Lett. **78**, 4063 (1997).
[61] A. Togo, F. Oba, and I. Tanaka, Phys. Rev. B **78**, 134106 (2008).
[62] B. Grabowski, T. Hickel, and J. Neugebauer, Phys. Rev. B **76**, 024309 (2007).
[63] Z.-G. Mei, S.-L. Shang, Y. Wang, and Z.-K. Liu, Phys. Rev. B **80**, 104116 (2009); C.-E. Hu, Z.-Y. Zeng, L. Zhang, X.-R. Chen, L.-C. Cai, and D. Alfè, J. Appl. Phys. **107**, 093509 (2010); Z.-G. Mei, Y. Wang, S.-L. Shang, and Z.-K. Liu, Inorg. Chem. **50**, 6996 (2011).
[64] A. J. Bard, R. Parsons, and J. Jordan, *Standard Potentials in Aqueous Solution* (Marcel Dekker, New York, 1985).
[65] J. Burgess, *Metal Ions in Solution* (Ellis Horwood Limited, Chichester, 1978).
[66] D. R. Lide, *CRC Handbook of Chemistry and Physics*, 90th ed. (CRC Press/Taylor and Francis, Boca Raton, FL, 2010).
[67] T. S. Mackey, JOM **46**, 59 (1994).
[68] D. V. Baubande, P. R. Menon, and J. M. Juneja, Indian J. Eng. Mater. Sci **9**, 275 (2002).
[69] D. Watanabe and J. R. Castles, Acta Crystallogr. **23**, 307 (1967); G. Eriksson and A. D. Pelton, Metall. Trans. B **24B**, 795 (1993); P. Waldner and G. Eriksson, Calphad **23**, 189 (1999); M. Cancarevic, M. Zinkevich, and F. Aldinger, *ibid.* **31**, 330 (2007); B. Jiang, N. Hou, S. Huang, G. Zhou, J. Hou, Z. Cao, and H. Zhu, J. Solid State Chem. **204**, 1 (2013); G. L. Humphrey, J. Am. Chem. Soc. **73**, 1587 (1951); A. D. Mah, K. K. Kelly, N. L. Gellert, E. G. King, and C. J. O'Brien, Thermodynamic Properties of Titanium-Oxygen Solutions and Compounds, Bureau of Mines Report of Investigations No. 5316, 1957 (unpublished); S. M. Ariya, M. P. Morozova, and E. Vol'f, Russ. J. Inorg. Chem. **2**, 16 (1957); T. V. Charlu, J. Chem. Thermodyn. **6**, 1065 (1974); G. V. Samsonov, *The Oxide Handbook* (IFI/Plenum Data Corporation, New York, 1973); O. Kubaschewski, C. B. Alcock, and D. J. Spencer, *Materials Thermochemistry* (Pergamon Press, Oxford, 1993).
[70] J. P. Perdew, J. A. Chevary, S. H. Vosko, K. A. Jackson, M. R. Pederson, D. J. Singh, and C. Fiolhais, Phys. Rev. B **46**, 6671 (1992).
[71] P. W. Gilles, P. J. Hampson, and P. G. Wahlbeck, J. Chem. Phys. **50**, 1048 (1969).
[72] A. Amtout and R. Leonelli, Phys. Rev. B **51**, 6842 (1995).
[73] R. R. Merritt and D. K. Philp, Philos. Trans. A **274**, 627 (1973).
[74] H. Gerischer, J. Electroanal. Chem. **82**, 133 (1977).
[75] C. Franchini, V. Bayer, R. Podloucky, J. Paier, and G. Kresse, Phys. Rev. B **72**, 045132 (2005).
[76] J. Paier, M. Marsman, K. Hummer, G. Kresse, I. C. Gerber, and J. G. Ángyán, J. Chem. Phys. **124**, 154709 (2006).
[77] C. Franchini, R. Podloucky, J. Paier, M. Marsman, and G. Kresse, Phys. Rev. B **75**, 195128 (2007).
[78] K. Hummer, A. Grüneis, and G. Kresse, Phys. Rev. B **75**, 195211 (2007).
[79] H. H. Wu and D. R. Trinkle, Phys. Rev. Lett. **107**, 045504 (2011).
[80] I. E. Grey, C. Li, I. C. Madsen, and G. Braunshausen, Mater. Res. Bull. **23**, 743 (1988).